Microgravity Science and Technology (2026) 38:7
https://doi.org/10.1007/s12217-026-10235-6

RESEARCH

# Effects of Gravity and Radiation on the Propagation of Spherically Expanding Ammonia/Air Flames

**Shize Du[1] · Yiqing Wang[1] · Shengkai Wang[1] · Zheng Chen[1]**

Received: 24 October 2025 / Accepted: 1 January 2026


**Abstract**

As a zero-carbon fuel, ammonia ($NH_3$) has attracted great interests recently. Due to its slow propagation speed, $NH_3$ flames are strongly affected by gravity and radiation. This study investigates the propagation of spherically expanding $NH_3$ /air flames under the combined effects of gravity and radiation using two-dimensional simulations with detailed chemistry and transport models. The results show that gravity significantly deforms the flame front, leading to a mushroom-shaped structure in which the local flame displacement speed varies along the front due to local stretch effects. This phenomenon becomes more pronounced at lower equivalence ratios as a result of the reduced flame speed. Overall, gravity enhances the global flame propagation speed. On the other hand, radiation slows the flame propagation by lowering the flame temperature and inducing an inward flow velocity. This makes the flame more susceptible to the influence of gravity and amplifies the deformation of the flame front. Finally, the performance of various approaches for determining the unstretched laminar flame speed from spherically expanding flames under gravitational and radiational conditions is assessed. It is found that when both gravity and radiation effects are significant, the spherically expanding flame method using flame radius history is not applicable, regardless of the definition of equivalent radius, and the surface-averaged method is the only reliable approach. This study provides insights into the understanding and accurate measurement of $NH_3$/air flame propagation characteristics.

**Keywords** Gravity · Radiation · Spherically expanding flame · Laminar flame speed · Ammonia

## Introduction

Ammonia ($NH_3$) is a carbon-free fuel and offers a promising response to the growing demand for clean energy driven by global warming and stringent carbon-emission limits (Glarborg et al. 2018; Kobayashi et al. 2019). $NH_3$ can be readily liquefied, transported, and stored under ambient conditions, and it benefits from a mature production and distribution infrastructure owing to its diverse industrial applications (Glarborg et al. 2018; Kobayashi et al. 2019). Despite these advantages, $NH_3$/air mixtures exhibit a high minimum ignition energy (Fernández-Tarrazo et al. 2023; Yu and Chen 2024), a narrow flammability range (Kobayashi et al. 2019; Zhou et al. 2021; Xie and Zhang 2025) and a slow laminar flame speed (typically <10 cm/s) (Takizawa et al. 2008; Hayakawa et al. 2015; Lhuillier et al. 2020). These features hinder prompt ignition and lengthen the ignition and early propagation period. In this weak and slow-flame regime, buoyancy-driven flows (Ronney 1998) and radiative heat losses (Chen 2010; Yu et al. 2014; Faghih et al. 2023; Glaznev et al. 2024) become significant and strongly affect both ignition and the subsequent flame propagation. This complicates the measurement of laminar flame speed (Chen 2015; Faghih and Chen 2016), a key property value that has been commonly used for chemical mechanism validation and the development of numerical models for turbulent premixed flames (Pitsch 2024). Accordingly, a systematic assessment of buoyancy and radiation effects on

✉ Shengkai Wang
sk.wang@pku.edu.cn

Shize Du
peterdu2000@pku.edu.cn

Yiqing Wang
wangyiqing@pku.edu.cn

Zheng Chen
cz@pku.edu.cn

[1] SKLTCS, HEDPS, School of Mechanics and Engineering Science, Peking University, Beijing 100871, China

Published online: 17 January 2026

$NH_3$/air flame propagation is essential for both fundamental understanding and practical implementation.

As reviewed in prior work (Glarborg et al. 2018; Kobayashi et al. 2019), substantial efforts have been devoted to $NH_3$ flames. The present study specifically focuses on measurements of the laminar flame speed using expanding spherical flames for $NH_3$/air mixtures. Using the spherically expanding flame method, Hayakawa et al. (2015) experimentally measured the laminar flame speed and Markstein length over a range of pressures. In their experiments, the slow $NH_3$/air flame deviated markedly from spherical symmetry owing to buoyancy. Following a similar approach, Zitouni et al. (2023) investigated the influences of hydrogen and methane addition on the laminar flame speed, Lewis number, and Markstein length of $NH_3$/air flames. Meanwhile, Chen et al. (2021) proposed a laminar flame parameter evaluation method based on the flame front evolution for the buoyancy-affected $NH_3$/air flames that were assumed to be quasi-ellipsoid, enabling measurements of laminar flame speed, Markstein length, and flame thickness across equivalence ratios and pressures. More recently, Mathew et al. (2025) developed a drop tower to investigate the spherically expanding flame of $NH_3$/air mixtures in free fall. Their results suggest that, for accurate determination of the laminar flame speed of slow $NH_3$/air mixtures, it is essential to eliminate gravity-induced natural convection and to account for radiation-induced inward flow. Collectively, these studies show that (i) the spherically expanding flame configuration is one of the most popular methods to measure the laminar flame speed of $NH_3$/air flames, and (ii) the flame deformation induced by buoyancy has largely limited the data range that can be used and considerably complicated the accurate measurement, especially when it is also subject to radiation effects. These observations have motivated the present study to investigate the spherically expanding $NH_3$/air flames under gravitational and radiational environments.

Several numerical studies have examined the deformation of slowly propagating spherical flames under gravitational conditions. Yakovenko and his coworkers (Yakovenko et al. 2018; Kiverin et al. 2019; Yakovenko et al. 2021) conducted a series of two-dimensional numerical simulations to study the structure and stability of ultra-lean $H_2$/air flames under gravity in the low-speed regime of spherical flames, revealing mushroom-shaped fronts with satellite kernels. Berger et al. (2020) simulated a lean $CH_4$/air flame and several fuel-rich $H_2$/air flames diluted with $N_2$ to investigate the sensitivities of buoyancy effects to laminar flame speed and Lewis number. In addition, they also evaluated the performance of five different techniques in determining the unstretched laminar flame speed, identifying the method based on surface-averaged quantities as the most accurate. Using the same two-dimensional cylindrical configuration, Wang et al. (2024) investigated the influence of buoyancy on the dimethyl ether cool flames and found that the volume-equivalent radius yields the best performance on extracting the laminar flame speed. These studies have yielded valuable insights into local flame dynamics under buoyancy-induced deformation and effective strategies for inferring the unstretched laminar flame speed from deformed flames. However, none of them have considered the $NH_3$/air flames. Furthermore, the coupling effects of buoyancy and radiation on the propagation of spherical $NH_3$/air flames have not been discussed.

To bridge the knowledge gap mentioned above, a series of two-dimensional simulations will be performed for the spherically expanding $NH_3$/air flames at gravitational and radiational environments. The objectives are twofold: (i) to investigate the influence of buoyancy and radiation on the propagation and structure of spherical $NH_3$/air flames; and (ii) to evaluate the performance of different techniques on the determination of laminar flame speed of $NH_3$/air flames with strongly deformed shape.

The remainder of this paper is organized as follows. Section "Model and Numerical Methods" details the model and numerical specifications utilized in the simulations. Section "Theoretical Background" presents the theoretical background for the flame speeds and some other key parameters. Section "Results and Discussion" outlines the numerical simulation results, first exploring gravity's role in $NH_3$/air flame propagation, then evaluating radiation's impact on mushroom-shaped flame propagation at gravitational environments. Additionally, the applicability of different fitting methods for extracting the unstretched laminar flame speed are compared and flame-propagation characteristics are analyzed quantitatively. Finally, Section "Conclusions" summarizes the main conclusions from this study.

## Model and Numerical Methods

As illustrated in Fig. 1, the flame ignition and propagation are stimulated in a quiescent flow field at gravitational environments. Three equivalence ratios are considered as $\phi = 0.7$, $0.8$ and $1.0$. The direction of gravity is vertically downward, and the radiation is either modeled using the optically thin model (OTM) or neglected (denoted as the adiabatic condition, ADI). The radiating species are selected as the polar molecules: $H_2O$, $NH_3$, NO and $N_2O$. Under

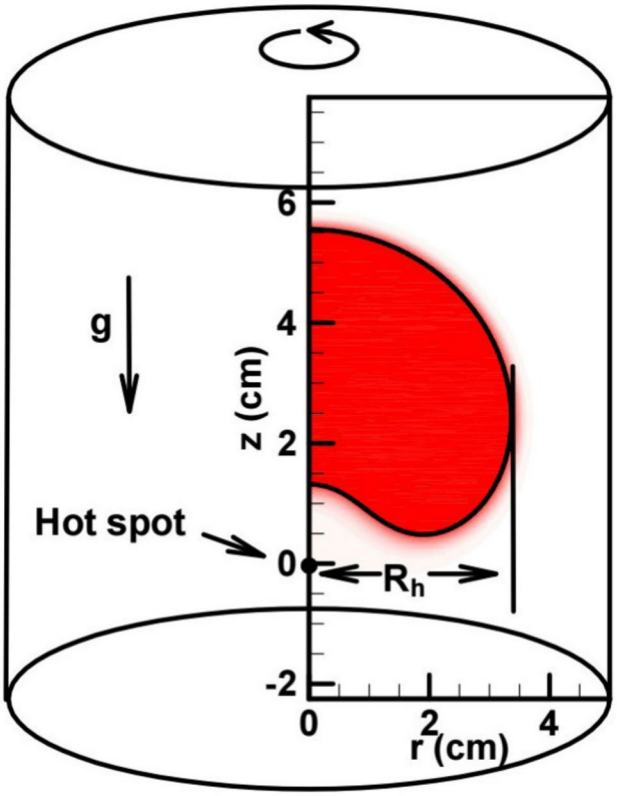


**Fig. 1** Schematic of computational domain and geometric parameters, including block settings, flame front and ignition positions, flame radius, cross-sectional area, and volume

the influence of gravity, the flame rises and stretches (Hayakawa et al. 2015; Zitouni et al. 2023) and ultimately forms an inwardly curling vortex structure (Mathew et al. 2025), and evolving into a mushroom-shaped flame with a concave base, which is depicted as the red region in Fig. 1.

The computational domain is defined in cylindrical coordinates $r - z$, with the $z$ axis as the axis of symmetry. The sizes are set to be $r \times z$ = 10.0 cm × 30.0 cm, 6.0 cm × 12.0 cm, and 15.0 cm × 30.0 cm for the three equivalence ratios, respectively. All external boundaries are open boundaries, employing the waveTransmissive boundary condition. The ambient temperature and pressure are set to 298 K and 1 atm, respectively. To ignite the flame, an ignition source is applied at the origin (0,0) in the initially quiescent flow field. For equivalence ratios of $\phi = 0.7$, 0.8 and 1.0, the ignition radius $R_{ig}$ is 1.0 mm, 0.5 mm, and 0.5 mm; the ignition duration $t_{ig}$ is 1.5 ms, 0.15 ms, and 0.15 ms; and the ignition power density $\epsilon_{ig}$ is $0.5\times10^{10}$ W/m$^3$, $1.0\times10^{10}$ W/m$^3$, and $1.0\times10^{10}$ W/m$^3$, respectively. Table 1 summarizes the key flame properties computed from one-dimensional planar premixed flames using Cantera (Goodwin et al. 2018).

Numerical simulations are conducted using the OpenFOAM-based solver EBIdnsFoam (Zirwes et al. 2020). The Navier-Stokes equations for a multi-component, reactive mixture are solved using the finite volume method. The mixture-averaged transport model (Curtiss and Hirschfelder 1949) is employed to compute the diffusion flux. A detailed $NH_3$ mechanism developed by Shrestha et al. (2021) is used. Chemical reaction terms are calculated using Sundials CVODE (Hindmarsh et al. 2005). The mesh is uniformly distributed, with the mesh size of $\Delta_x$= 200, 80, and 80 μm for the three equivalence ratios, respectively, ensuring that there are more than 20 grids within one laminar flame thickness $l_F$ (see Table 1). The grid convergence is verified by comparing results with those from twice-as-dense meshes. The time step is controlled using a CFL number of 0.2, with a maximum time step of $2 \times10^{-6}$ s.

In addition to the gravity cases, six zero-gravity cases are computed for comparison. In these zero-gravity runs, the lower boundary condition is changed to a symmetry boundary. This allows the ignition kernel to be relocated to the lower boundary, reducing the computational cost. All other simulation settings are identical to those used with gravity.

## Theoretical Background

To quantitatively analyze the effects of gravity and radiation on $NH_3$/air flames, this section begins by introducing three distinct methodologies for extracting unstretched laminar flame speed $S^0_{L,u}$ from deformed flames. Then, two critical dimensionless quantities will be discussed. One is the Markstein number *Ma*, which quantifies the response of laminar flame speed to stretch, and the other is the Richardson number *Ri*, which assesses the degree of flame deformation caused by gravity.

**Table 1** Unstretched flame properties at different equivalence ratios. $\rho_u$ and $\rho_b$ are densities of the unburned and burned mixtures, respectively. $S^0_{L,u}$ is the unstretched laminar flame speed, and $l_F$ is the unstretched laminar flame thickness, defined as $l_F = (T_{ad} - T_u)/\max(|\nabla \mathrm{T}|)$. Here, $T_u$ and $T_{ad}$ represent the unburned mixture and adiabatic flame temperatures, respectively, and $\max(|\nabla \mathrm{T}|)$ denotes the maximum temperature gradient. The definitions of *Ma* will be given in Section "Theoretical Background"

| $\phi$ | $\rho_u$ (kg/m$^3$) | $\rho_b$ (kg/m$^3$) | $S^0_{L,u}$ (cm/s) | $T_{ad}$ (K) | $l_F$ (mm) | *Ma* |
|---|---|---|---|---|---|---|
| 0.7 | 1.10 | 0.18 | 2.62 | 1727 | 4.07 | 4.55 |
| 0.8 | 1.09 | 0.17 | 4.03 | 1855 | 2.91 | 5.15 |
| 1.0 | 1.07 | 0.15 | 6.85 | 2060 | 2.03 | 6.43 |

## Laminar Flame Speed Determination

### Method 1: Based on Equivalent Radius

The most straightforward approach to obtain the unstretched laminar flame speed $S^0_{L,u}$ from the mushroom-shaped flame is following the spherically expanding flame method, where $S^0_{L,u}$ is derived from the flame radius history $R = R(t)$. Detailed information about this method can be found in Chen (2015), and thus it is only briefly described here.

First, given the burned gas inside the spherical flame front is quiescent, the stretched flame speed with respect to the burned gas $S_{L,b}$ can be obtained from the time derivative of the flame radius (Chen 2010; Mathew et al. 2025):

$$S_{L,b} = \frac{dR}{dt} \tag{1}$$

On the other hand, it is usually assumed that $S_{L,b}$ is influenced by the flame stretch rate $K$ following the linear correlation (Mathew et al. 2025; Clavin 1985; Bechtold and Matalon 2001; Giannakopoulos et al. 2015):

$$S_{L,b} = S^0_{L,b} - L_b K \tag{2}$$

where $S^0_{L,b}$ is the unstretched flame speed with respect to the burned gas and $L_b$ is the burnt Markstein length, a constant quantifying how the flame speed $S_{L,b}$ is influenced by the stretch rate $K$ (Bechtold and Matalon 2001; Giannakopoulos et al. 2015). $L_b$ will be further elaborated in Section "Markstein Length".

The flame stretch rate $K$ is defined as the temporal rate of change of the flame front surface area $A$ per unit area: Mathew et al. (2025); Dowdy et al. (1991):

$$K = \frac{1}{A}\frac{dA}{dt} \tag{3}$$

For a spherical flame, the stretch rate $K$ is uniform over the flame front due to spherical symmetry. By substituting $A = 4\pi R^2$ into the equation, the relationship between $K$ and $R$ can be expressed as:

$$K = \frac{2}{R}\frac{dR}{dt} \tag{4}$$

Given Eqs. 1 and 4, $S^0_{L,b}$ can be obtained by extrapolating from the linear fitting of Eq. 2, and the unstretched laminar flame speed $S^0_{L,u}$ can then be calculated based on the mass conservation as Mathew et al. (2025); Tavares et al. (2023):

$$S^0_{L,u} = S^0_{L,b} \cdot \frac{\rho_u}{\rho_b} \tag{5}$$

where $\rho_b$ and $\rho_u$ denote the densities of the burnt and unburnt mixtures, respectively. Accordingly, the stretched flame speed with respect to the unburned gas $S_{L,u}$ can be expressed as:

$$S_{L,u} = S^0_{L,u} - L_u K \tag{6}$$

where $L_u = L_b \rho_u / \rho_b$ is the unburnt Markstein length.

To apply this method to $NH_3$/air flames at gravitational environments, an equivalent flame radius should be determined for the mushroom-shaped flames. In this study, three distinct types of equivalent radii are considered, which are listed in Table 2. Specifically, the subscript *h* indicates that the equivalent radius of the mushroom-shaped flame is determined by the maximum horizontal extension of the flame front. The subscript *eqCR* signifies that the equivalent radius corresponds to the radius of a semicircle in the $r - z$-plane, which has the same projected area as the flame. Meanwhile, the subscript *eqV* denotes that the equivalent radius is that of a sphere with a volume equal to that of the flame region. In a zero-gravity environment, the above three definitions would lead to the same value, which is denoted by the subscript 0*g*.

These three equivalent radii evaluate the flame speed through the geometrical properties of the flame, which can be conveniently obtained from Schlieren images in experiments. Correspondingly, in simulations, they can also be obtained from the flame front location. In this study, the iso-surface of $H_2O$ mass fraction $Y_{H_2O}$ is selected to identify the flame front, following the same choice adopted in Yao and Blanquart (2024). Specifically, the iso-value of $Y_{H_2O}$ corresponds to the maximum of the gradient $dY_{H_2O}/dx$ in the one-dimensional unstretched laminar flame. Note that in Giannakopoulos et al. (2015), it was found that the correlation between flame speed and flame stretch is insensitive to the choice of iso-surface as long as the iso-surface is sufficiently close to the burned side of the flame. Specifically, their results suggest that an iso-surface corresponding to a normalized temperature of $T^* = T/T_u > 4$ can be regarded as sufficiently close to the burned side. In the present study, the iso-surfaces selected in the flame cases of $\phi =$ 1.0, 0.8, and 0.7 correspond to temperatures of 1349, 1345, and 1308 K, respectively; and for all these cases, $T^* > 4$ applies.

**Table 2** Definitions of different equivalent radii

| Abbreviation | Radius description |
|---|---|
| h | Maximum-horizontal-extension equivalent radius under 1g gravity |
| eqCR | Areal equivalent radius under 1g gravity |
| eqV | Volumetric equivalent radius under 1g gravity |
| 0g | Radius under zero gravity |

### Method 2: Based on Flame Displacement Speed

This subsection presents the second method for determining the unstretched laminar flame speed $S^0_{L,u}$ from a deformed flame. Instead of employing equivalent radii, each point on the deformed flame front is considered to account for the significant variations in the local flame properties. To this end, the flame displacement speed $S_d$ of an iso-surface is examined (Giannakopoulos et al. 2015), which represents the speed of this iso-surface relative to the flow (Berger et al. 2020; Poinsot and Veynante 2005):

$$S_d = \frac{1}{|\nabla\Theta|}\frac{\partial\Theta}{\partial t} + \vec{u}\cdot\frac{\nabla\Theta}{|\nabla\Theta|} \tag{7}$$

where $\Theta$ denotes the field quantity used to calculate the iso-surface, and $\vec{u}$ represents the flow speed. For a flame front defined by the iso-surface of $Y_{H2O}$, the expression for $S_d$ is written as follows:

$$S_d = \frac{1}{|\nabla Y_{H_2O}|}\frac{\partial Y_{H_2O}}{\partial t} + \vec{u}\cdot\frac{\nabla Y_{H_2O}}{|\nabla Y_{H_2O}|} \tag{8}$$

Consider the governing equation for the $H_2O$ species below:

$$\rho\left(\frac{\partial Y_{H_2O}}{\partial t} + \vec{u}\cdot\nabla Y_{H_2O}\right) = \nabla\cdot(\rho D_{H_2O}\nabla Y_{H_2O}) + \omega_{H_2O} \tag{9}$$

where, $D_{H_2O}$ and $\omega_{H_2O}$ represent the diffusion coefficient and reaction rate of $H_2O$, respectively. As such, the displacement speed $S_d$ can be written as the sum of the diffusion term and the reaction term (Berger et al. 2020; Poinsot and Veynante 2005):

$$S_d = \frac{\nabla\cdot(\rho D_{H_2O}\nabla Y_{H_2O})}{\rho|\nabla Y_{H_2O}|} + \frac{\omega_{H_2O}}{\rho|\nabla Y_{H_2O}|} \tag{10}$$

The influence of local flame stretch rate on $S_d$ can be divided into two parts: the effects of strain and curvature on the flame (Bechtold and Matalon 2001; Clavin and Graña-Otero 2011; Thiesset et al. 2017):

$$S^*_d = S^0_{L,u} - L_{K_s}K_s - L_\kappa S^0_{L,u}\kappa \tag{11}$$

where, $S^\star_d = \rho/\rho_u S_d$ denotes the density-weighted displacement speed, which accounts for the local density $\rho$ in weighting the displacement speed $S_d$. $K_s = -\vec{n}\cdot\nabla\vec{u}\cdot\vec{n} + \nabla\cdot\vec{u}$ represents the strain rate on the flame front, and $\kappa = \nabla\cdot\vec{n}$ denotes the curvature of the flame front. Here, $\nabla\vec{u}$ is the strain rate tensor (Candel and Poinsot 1990) and $\vec{n}$ is the outward vector normal to the flame front, i.e., $\vec{n} = \nabla Y_{H_2O}/|\nabla Y_{H_2O}|$ (Poinsot and Veynante 2005). Their relationship with the stretch rate $K$ is:

$$K = K_s + S_d\kappa \tag{12}$$

Additionally, $L_{K_s}$ and $L_\kappa$ are the Markstein lengths associated with strain rate and curvature, respectively. Their physical meanings quantify how the flame speed is affected by strain rate and curvature (Clavin and Graña-Otero 2011). According to Eq. 11, for a deformed flame propagating steadily, plotting the data points of density-weighted displacement speed $S^\star_d$ versus the strain rate $K_s$ and curvature $\kappa$ in a three-dimensional space yields a plane. Consequently, intersecting the plane fitted from these data points with the $S^\star_d$-axis, the height of the intersection point represents the laminar flame speed $S^0_{L,u}$. Simultaneously, $S^0_{L,b}$ can also be calculated through Eq. 5. This constitutes the second method to determinate laminar flame speed, also known as the three-dimensional planar fitting method.

### Method 3: Based on Surface-Averaged Quantities

The third method is known as the surface-averaged method (Berger et al. 2020; Vervisch et al. 1995). Similar in principle to the three-dimensional planar fitting method, the surface-averaged method differs in that it performs a weighted average of the data on the flame front at each moment. On the flame front defined by the iso-surface of $Y_{H2O}$, the magnitude of the $H_2O$ mass-fraction gradient $|\nabla Y_{H_2O}|$ reflects local spatial variations in the $H_2O$ production rate, so that when the production at a point exceeds that of its surroundings, a large $|\nabla Y_{H_2O}|$ will develop in its vicinity. Therefore, $|\nabla Y_{H_2O}|$ is used to weight various physical quantities $\psi$ :

$$\mathcal{A} = \int_f |\nabla Y_{H_2O}|\, dS \tag{13}$$

$$\hat{\psi} = \frac{1}{\mathcal{A}}\int_f \psi\,|\nabla Y_{H_2O}|\, dS \tag{14}$$

Here, $\mathcal{A}$ represents the normalization factor for weighting, signifying the total combustion intensity across the entire flame front. The symbol $\psi$ can denote any physical quantity, such as $S^\star_d$, $K_s$, or $\kappa$, and $\hat{\psi}$ denotes the result after surface averaging. Subsequently, a planar fit is performed on the data points ($\hat{S}^\star_d$, $\hat{K}_s$, $\hat{\kappa}$) at different moments, which constitutes the procedure of the surface-averaged method.

In Section "Measurement of Unstretched Laminar Flame Speed", the three methods to determine the laminar flame speed $S^0_{L,u}$ of $NH_3$/air flames under gravitational and radiational environments will be compared and analyzed.

### Markstein Length

For flames where the propagation speed is affected by the stretch rate, the coefficient quantifying the stretch rate's effect on flame speed has a dimension of length (Bechtold and Matalon 2001; Giannakopoulos et al. 2015) and is termed the Markstein length. According to asymptotic theory, the Markstein length on the burned gas side can be calculated using a theoretical formula (Bechtold and Matalon 2001; Giannakopoulos et al. 2015; Okafor et al. 2014):

$$Ma = \frac{2}{\sqrt{\sigma}+1} + \frac{2Ze\left(Le_{eff}-1\right)}{\sigma-1}\left\{\sqrt{\sigma}-1-ln\frac{\sqrt{\sigma}+1}{2}\right\} \tag{15}$$

where $\sigma = \rho_u/\rho_b$, $Ze$ is the Zel'dovich number (Okafor et al. 2014; Gaucherand et al. 2023; Müller et al. 1997; Sun et al. 1999), representing the normalized activation energy of the overall reaction, and $Le_{eff}$ is the effective Lewis number of the unburned gas. The Zel'dovich number is calculated based on the sensitivity of the adiabatic flame temperature to the flow rate (Gaucherand et al. 2023):

$$Ze = -2\frac{d\left(\rho_u \cdot S^0_{L,u}\right)}{d\left(\frac{1}{T_{ad}}\right)} \cdot \frac{T_{ad}-T_u}{T^2_{ad}} = 2\left(T_{ad}-T_u\right)\frac{d\left(\rho_u \cdot S^0_{L,u}\right)}{d\left(T_{ad}\right)} \tag{16}$$

and effective Lewis number can be calculated as Okafor et al. (2014); Gaucherand et al. (2023); Müller et al. (1997); Sun et al. (1999); Joulin and Mitani (1981):

$$Le_{eff} = \begin{cases} \frac{Le_O + A\cdot Le_F}{1+A}, A = 1+Ze\left(\phi^{-1}-1\right) & \text{if } \phi < 1 \\ \frac{Le_F + A\cdot Le_O}{1+A}, A = 1+Ze\left(\phi-1\right) & \text{if } \phi > 1 \end{cases} \tag{17}$$

Here, $Le_F$ and $Le_O$ denote the Lewis numbers of the fuel and oxidant, respectively. When $Ma > 0$, the flame is promoted if $K < 0$ and inhibited if $K > 0$. Conversely, when $Ma < 0$, the opposite conclusions hold (Chen et al. 2009). Note that Ma computed using Eq. 15 is mainly used as an indicator of whether the flame speed is positively or negatively correlated with the flame stretch rate.

### Richardson Number

Under gravity's influence, slowly propagating flames deform into mushroom-liked shapes and rise upward rather than remaining spherical. The Richardson number *Ri* quantifies buoyancy's effect on the flame (Berger et al. 2020; Wang et al. 2024; Mathew et al. 2025; Choi et al. 2016; Law et al. 1980):

$$Ri = \frac{\rho_u - \rho_b}{\rho_u}\frac{gR}{\left(\frac{dR}{dt}\right)^2} \tag{18}$$

where $g$ is the gravitational acceleration constant and $R$ denotes different equivalent radii. Significant flame deformation is observed when $Ri > 1$ (Berger et al. 2020; Mathew et al. 2025).

## Results and Discussion

### Effects of Gravity on Flame Propagation

In this subsection, the effects of gravity on the propagation of $NH_3$/air flames are first examined without considering radiation. Figure 2 presents the evolution of mushroom-shaped flames at different times for $\phi$ =0.7, 0.8, and 1.0, with the distribution of normalized displacement speed $S^\star_d/S^0_{L,u}$ superimposed on the flame front. Following ignition, thermal runaway initiates a small spherical flame kernel that rises under the influence of gravity. The density

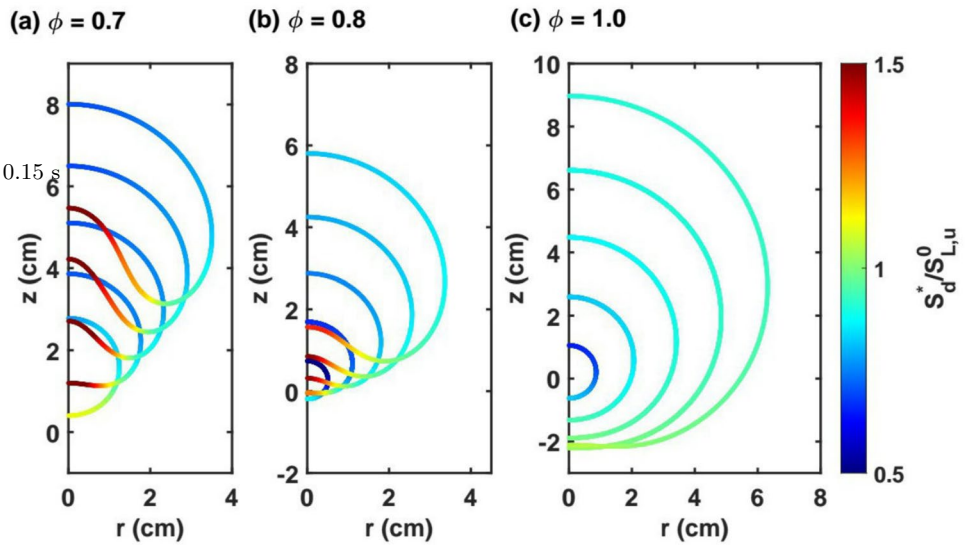


**Fig. 2** Temporal evolutions of density weighted displacement speed $S^\star_d$ normalized by unstretched planar unburnt flame speed $S^0_{L,u}$ for cases at (**a**) $\phi = 0.7$, (**b**) $\phi = 0.8$, and (**c**) $\phi = 1.0$ at time instances $t = 0.03$ s, 0.06 s, 0.09 s, 0.12 s and 0.15 s

gradient points from the burned gas region toward the unburned gas, while the pressure-gradient vector is directed opposite to gravity. Then, the vorticity is generated by the misalignment between the pressure and density gradients, i.e., $\frac{d\vec{\omega}}{dt} = \frac{1}{\rho^2}\nabla\rho \times \nabla \mathrm{p}$ (Wu et al. 2015). As the flame rises, a clockwise vortex develops on the outer side of the flame, driving the transition from a spherical to a characteristic mushroom-shaped structure.

In Fig. 2a for $\phi = 0.7$, $S_d^\star/S_{L,u}^0$ is greater than unity in the lower region of the flame and less than unity in the upper region. Since the local flame reactivity is strongly influenced by the local flame stretch rate, Fig. 3 presents the distribution of the Karlovitz number *Ka* superimposed on the flame front for the corresponding cases and time instants. Here, *Ka* is the dimensionless stretch rate, normalized by the laminar flame speed and the flame thickness: $Ka = K \cdot \delta_T/S_{L,u}^0$. As shown in Fig. 3a, regions exhibiting large (small) $S_d^\star/S_{L,u}^0$ correspond to locations where *Ka* is significantly negative (positive). This correlation is consistent with the Markstein number reported in Table 1: with a positive Markstein number, positive stretch rates suppress flame propagation, whereas negative stretch rates enhance it. Although similar behavior is observed in Fig. 2b and 2c, the effect is less pronounced than that in Fig. 2a. This is attributed to the higher $S_{L,u}^0$ for $\phi$=0.8 and 1.0, which reduces the sensitivity of the flame to gravity and consequently mitigates deformation.

Figure 4 presents the distribution of $S_d^\star/S_{L,u}^0$ and its two components, the diffusion term and the reaction term (see Eq. 10), along the flame front for the three mushroom-shaped flames at the same time instant $t = 0.15$ s. The *x*-coordinate $l$ denotes the normalized flame length measured from the flame upper tip. The comparison indicates that the influence of gravity becomes more pronounced at lower equivalence ratios. For locations where $l$ 0.6, the diffusion term increases significantly, while the chemical reaction term decreases slightly. This behavior suggests that the enhancement of the displacement speed in the concave region near the flame base is primarily attributed to the increase in the diffusion contribution.

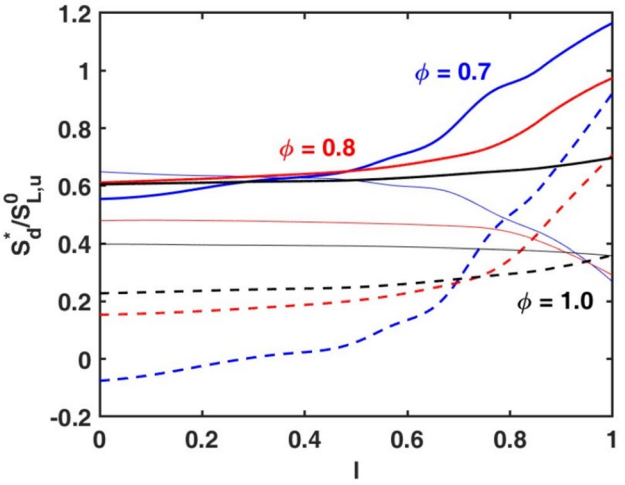


**Fig. 4** Variation of normalized density weighted displacement speed $S_d^\star/S_{L,u}^0$ versus normalized flame front length $l$ in the clockwise direction for cases $\phi = 0.7$ and 0.8 at the same time instance $t = 0.15$. The solid, dashed and thin lines indicate density weighted displacement speed, its diffusion part and reaction part respectively

To examine the overall propagation speed of these flames, Fig. 5(a-c) show the evolution of burned flame speed $S_{L,b}$ as a function of equivalent radius for different equivalence ratios. Here, $S_{L,b}$ is obtained using the method presented in Section "Method 1: Based on Equivalent Radius", i.e., Eq. 1. The results from the three different definitions of equivalent radius, i.e., $R_h$, $R_{eqCR}$, and $R_{eqV}$, are compared, while the corresponding zero-gravity flame is included for reference. In all cases, $S_{L,b}$ initially decreases with *R* due to the dissipation

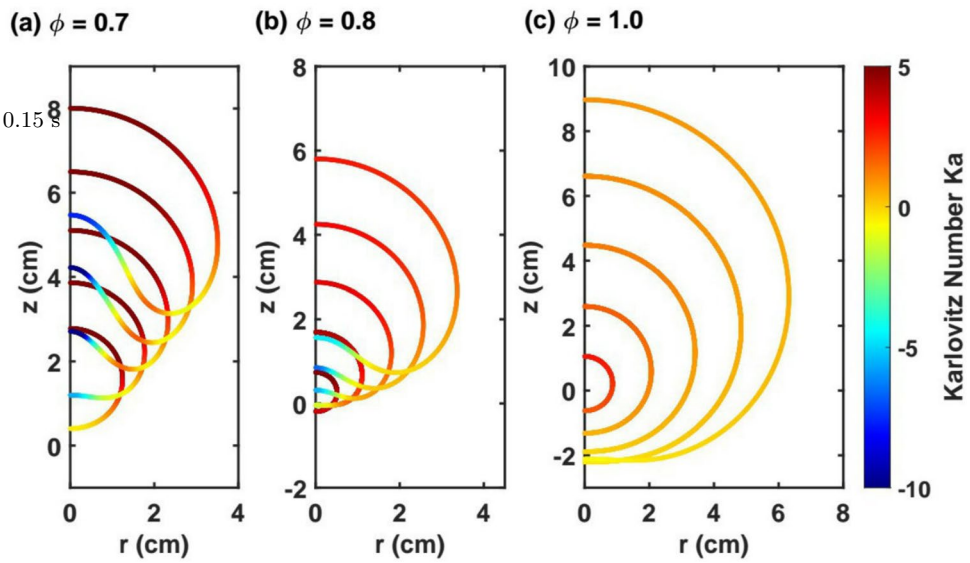


**Fig. 3** Temporal evolutions of Karlovitz number Ka for cases at (**a**) $\phi = 0.7$, (**b**) $\phi = 0.8$, and (**c**) $\phi = 1.0$ at time instances $t = 0.03$ s, 0.06 s, 0.09 s, 0.12 s and 0.15 s

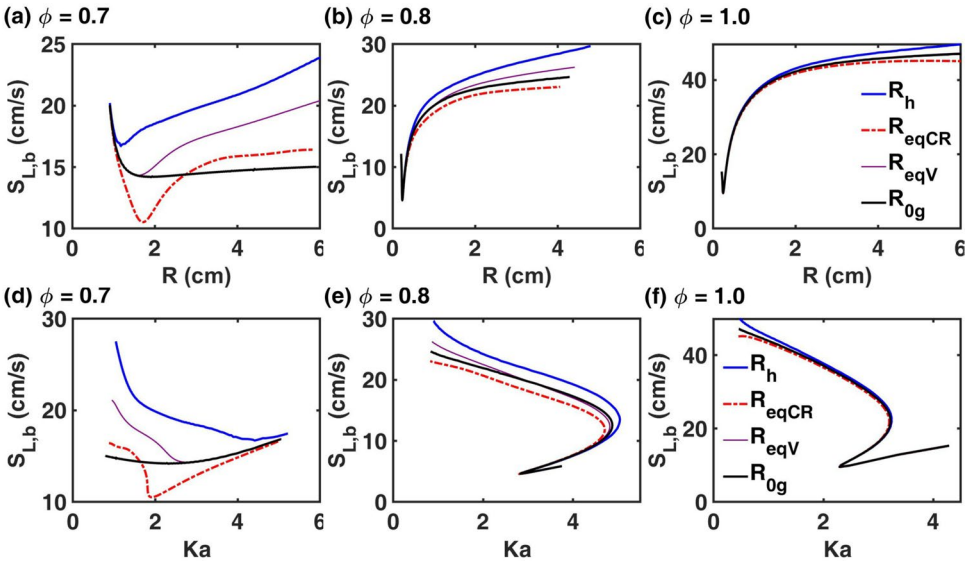


**Fig. 5** Variation of burned flame speed $S_{L,b}$ with flame equivalent radii $R$ (**a**, **b**, **c**) and Karlovitz number $Ka$ (**d**, **e**, **f**) for adiabatic cases

of ignition energy. Subsequently, it increases sharply with $R$ in the beginning, followed by a gradual decrease in the growth rate. The latter usually indicates that the flame has reached a quasi-steady propagation stage.

This behavior is more clearly illustrated in Fig. 5(d-f), where $S_{L,b}$ is replotted as a function of the stretch rate $K$. Here, $K$ is computed from the equivalent radius $R$ (see Eq. 4) and represents the overall stretch rate of the entire flame front. Note that as the flame evolves, $R$ increases while $K$ decreases. For $\phi$=0.8 and 1.0, $S_{L,b}$ increases almost linearly with the decreasing $Ka$ at the later stage, with the negative slope consistent with the positive Markstein number reported in Table 1. However, the $S_{L,b}$-$Ka$ curves deviate from linearity toward the end of the simulation, as the flame front becomes increasingly distorted by gravity and departs from spherical symmetry eventually. At lower $\phi$, the influence of gravity is stronger, leading to more pronounced deviations. As shown in Fig. 5(d), for $\phi$ = 0.7 where the flame front is significantly deformed at much earlier time than higher $\phi$ cases, a linear region is hardly observed. Such deviations inevitably hinder the accurate measurement of $S^0_{L,u}$, as will be further discussed in Section "Measurement of Unstretched Laminar Flame Speed". Finally, it is also observed that for the deformed flames at $\phi$ = 0.7 and 0.8, the $S_u$ values obtained from $R_{eqV}$ are higher than those from the zero-gravity flame, indicating that gravity accelerates the overall flame propagation. This acceleration is primarily attributed to the locally increased flame reactivity observed in the negatively stretched regions of the mushroom-shaped flame.

Figure 6 further shows the temporal evolution of the Richardson number $Ri$ calculated from Eq. 18 for different equivalence ratios. $Ri$ characterizes the extent of flame deformation under gravity. As reported by Berger et al. (2020), a sufficiently large $Ri$ indicates the onset of significant deformation. In the present study, for $\phi = 0.7$, $Ri$ exceeds 4 shortly after ignition, at approximately $t = 0.02$ - $0.03$ s. In contrast, for $\phi$ = 0.8 and 1.0, $Ri$ remains below this threshold throughout the evolution. These results suggest that, for the $NH_3$/air flames considered in this study, $Ri$ is still an effective indicator of gravity-induced deformation, with a potential critical range of $Ri \approx 4-6$.

## Combined Effects of Gravity and Radiation

In this subsection, the influence of radiation is considered. Figure 7 first shows the flame propagation process for $NH_3$/air flames with $\phi$=0.7 in gravitational and zero-gravity environments. It is observed that, in the absence

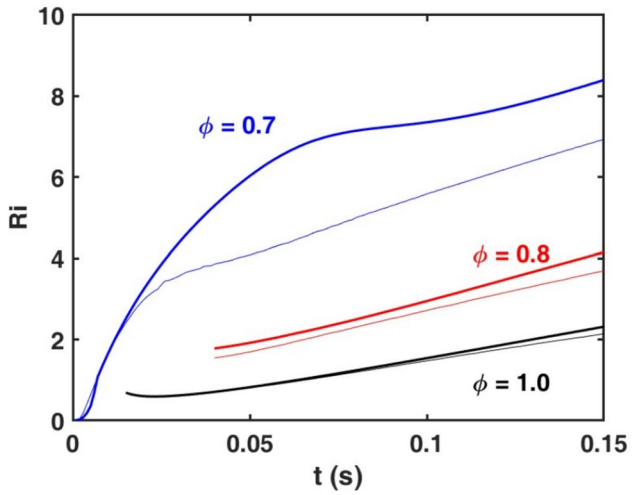


**Fig. 6** Temporal evolutions of Richardson number $Ri$ for adiabatic cases. The blue, red, and black lines represent results for $\phi = 0.7$, 0.8 and 1.0 respectively. The thick and thin lines indicate flame speeds obtained from $R_h$ and $R_{eqV}$, respectively

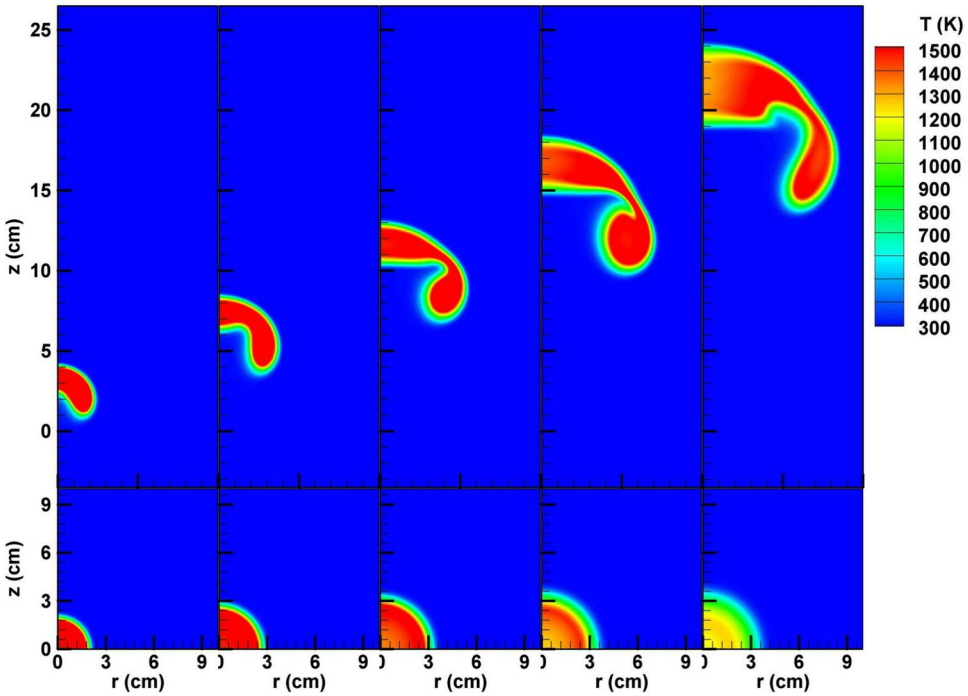


**Fig. 7** Contour maps for temporal evolutions of temperature distribution at an equivalence ratio of $\phi = 0.7$ under the OTM radiation model for both 1g (top) and 0g (bottom) conditions at $t$ = 0.1, 0.2, 0.3, 0.4 and 0.5 s

of gravity, ignition fails, as indicated by the decreasing temperature in the burned region of the spherical flame. In contrast, when gravity is present, the initial flame kernel becomes significantly deformed, forming an inward-concave structure with a negative flame stretch rate. This negative stretch promotes flame propagation, as discussed in the previous section, ultimately leading to a successful ignition. These results demonstrate that radiation-induced heat loss inhibits flame propagation, while gravity-induced negative stretch enhances it. The competition between these two effects becomes increasingly critical as the mixture approaches the flammability limit. For $NH_3$/air flames with $\phi$=0.8 and 1.0, ignition can always be achieved under radiational conditions, regardless of the presence of gravity.

To examine the influence of radiation on the flame propagation, Fig. 8 presents the temporal evolution of the flame front, superimposed with the normalized displacement speed $S_d^\star/S_{L,u}^0$ and the Karlovitz number $Ka$ (i.e., the normalized stretch rate) for $\phi = 0.8$. Results from both the radiational and adiabatic cases are shown for direct comparison. Note that the $S_{L,u}^0$ used for normalization is computed using Cantera with the OTM radiation model and the adiabatic model, respectively. It is found that radiation noticeably slows down the overall flame propagation, as evidenced by the smaller flame size in the radiative case compared with the adiabatic case at the same time instant. Two mechanisms are responsible for this suppression. First, the radiation-induced heat loss reduces temperature

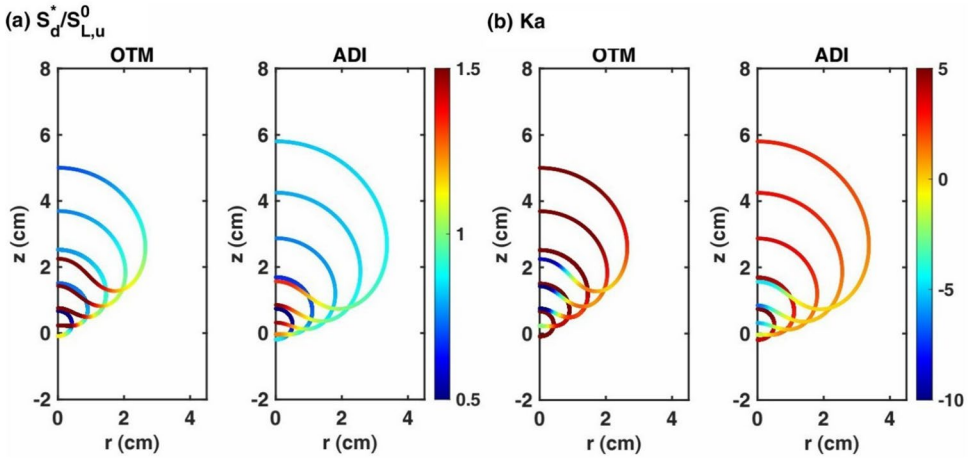


**Fig. 8** Temporal evolutions of (**a**) density weighted displacement speed $S_d^\star$ normalized by unstretched planar unburnt flame speed $S_{L,u}^0$ and (**b**) Karlovitz number $Ka$ for OTM model and adiabatic condition at time instances $t$ = 0.03 s, 0.06 s, 0.09 s, 0.12 s, and 0.15 s

within the flame, as illustrated in Fig. 9, which shows the temperature fields at $t$ = 0.15 s for both cases. The lower flame temperature weakens the flame reactivity, resulting in a smaller flame speed (i.e., lower $S^0_{L,u}$). Second, the reduced temperature in the burned gas region results in an increase in the local density, inducing an inward flow that further retards flame propagation. Similar radiation-induced inward flow phenomena have also been reported in previous studies (Faghih et al. 2023; Mathew et al. 2025; Wang et al. 2022).

Since radiation reduces the overall flame propagation speed, the flame becomes more susceptible to effects of gravity. This can be seen from the greater deformation of the radiational flame compared with the zero-gravity flame, as shown in Fig. 8. Consequently, the flame experiences stronger stretch, and the variations in local flame speed ($S^\star_d/S^0_{L,u}$) along the flame front are more significant for the radiational flame.

Finally, the impact of radiation on the relationship between flame speed and stretch rate is examined. Figure 10 shows the variation of $S_{L,b}$ with $Ka$ for $NH_3$/air flames at $\phi$ = 0.8 and 1.0 under gravitational conditions. Here, the normalization parameters are computed using Cantera with the OTM model. A comparison of Figs. 5 and 10 reveals that radiation introduces significant non-linearity in the low-stretch-rate region, i.e., when the flame is sufficiently large. Specifically, for $R_{eqCR}$, $R_{eqV}$, and $R_{0g}$, the curves exhibit a clear downward warp with decreasing $Ka$, resulting from the reduced flame propagation speed and the inward flow velocity $u_b$ induced by radiative heat loss. This non-linearity inevitably presents additional challenges for extrapolating the unstretched laminar flame speed from the spherically expanding flame method. In contrast, the curve for $R_h$ appears nearly linear; however, this linearity arises because the acceleration effect from gravity (see Fig. 5) offsets the suppression effect from radiation. Therefore, it does not guarantee that $R_h$ will exhibit good performance in determining the unstretched laminar flame speed, as will be further discussed in the next section.

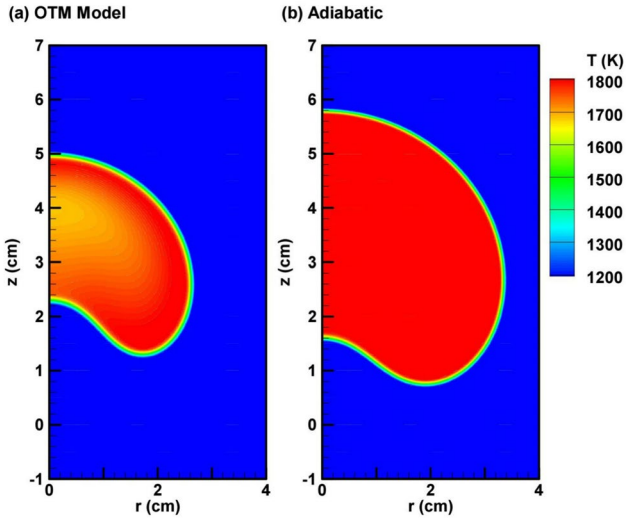


**Fig. 9** Contour maps for temperature distributions (**a**) using OTM model and (**b**) at adiabatic conditions at an equivalence ratio of $\phi = 0.8$ at $t$ = 0.15 s

## Measurement of Unstretched Laminar Flame Speed

In this study, three definitions of equivalent radius and three methods to extract the unstretched laminar flame speed $S^0_{L,u}$ are considered, which yields a total of five different estimates.

For the methods based on the equivalent radius, the adiabatic case with $\phi$ = 0.8 is taken as an example to illustrate the linear extrapolation procedure in Fig. 11. Specifically, for each curve, the portion exhibiting good linearity is selected and extrapolated to zero stretch rate to obtain $S^0_{L,b}$. The unstretched laminar flame speed $S^0_{L,u}$ is then calculated using Eq. 5. It is worth noting that, because the curve derived from $R_h$ is more sensitive to the effects of gravity than the other two definitions, the

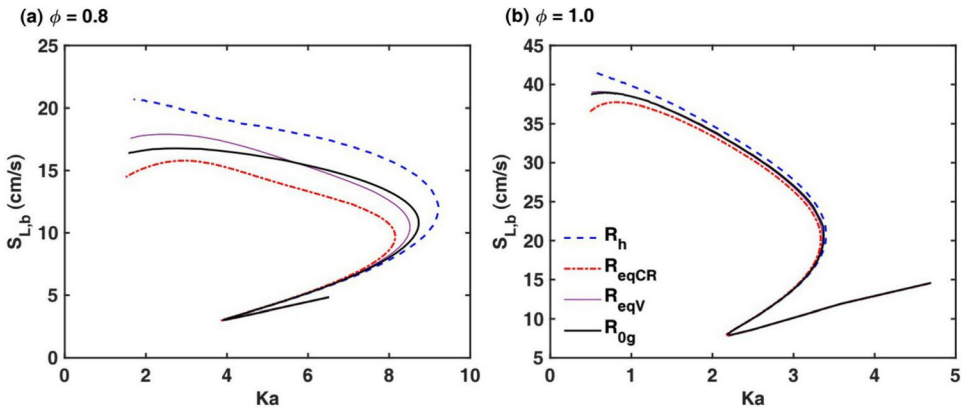


**Fig. 10** Variations of burned flame speed $S_{L,b}$ with Karlovitz number $Ka$ at (**a**) $\phi = 0.8$ and (**b**) $\phi = 1.0$, respectively

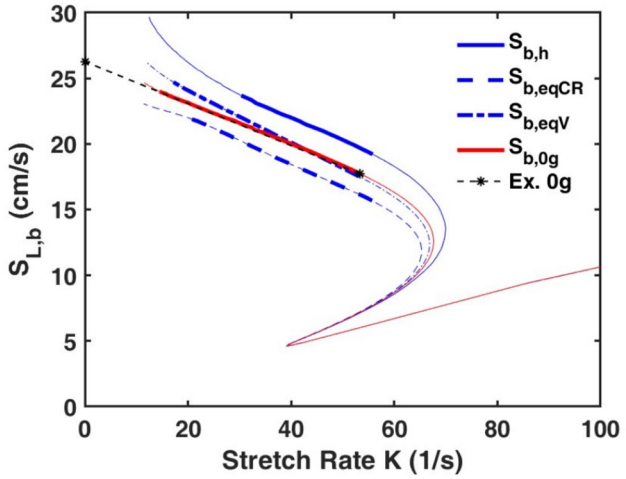


**Fig. 11** Variation of burned flame speed $S_{L,b}$ with Stretch $K$ for fitting $S^0_{L,u}$ for $\phi$=0.8 at adiabatic conditions. The thin lines show the full dataset, and the thick lines indicate the linear portions used to fit $S^0_{L,u}$. The black dashed lines marked with asterisks illustrate example line segments obtained by extrapolating fits to the selected data from the zero-gravity case

range of data suitable for extrapolation is correspondingly narrower.

Figure 12 presents the fitting planes obtained using the three-dimensional planar fitting method and the surface-averaged method, respectively, for the same case shown in Fig. 11. It is observed that most of the data lie closely on a single planar plane, demonstrating the validity of these two methods.

Table 3 summarizes the $S^0_{L,u}$ values obtained using different methods under adiabatic and radiative conditions. Here, 3*DPlane* refers to the three-dimensional planar fitting method, and *SA* denotes the surface-averaged method. The accuracy of each method is evaluated based on its ability to reproduce the gravity-free reference value. Accordingly, the measurement error is calculated using the $S^0_{L,u}$ obtained from $R_{0g}$ as the reference.

**Table 3** Unstretched laminar flame speeds $S^0_{L,u}$ obtained from different methods and their errors. The first two columns of data are from the adiabatic cases, while the last two columns are from the radiational cases

| $\phi$ | Method | $S^0_{L,u}$ (cm/s) | Error (%) | $S^0_{L,u}$ (cm/s) | Error (%) |
|---|---|---|---|---|---|
| 0.7 | $R_{0g}$ | 2.60 | - | | |
| | $R_h$ | 4.06 | 55.9 | | |
| | $R_{eqCR}$ | 3.64 | 39.7 | | |
| | $R_{eqV}$ | 3.73 | 43.5 | | |
| | 3D Plane | 2.78 | 6.8 | | |
| | SA | 2.73 | 5.1 | | |
| 0.8 | $R_{0g}$ | 4.06 | - | 2.85 | - |
| | $R_h$ | 4.44 | 9.5 | 3.46 | 21.4 |
| | $R_{eqCR}$ | 3.95 | -2.8 | 3.04 | 6.7 |
| | $R_{eqV}$ | 4.31 | 6.3 | 3.43 | 20.4 |
| | 3D Plane | 4.28 | 5.6 | 3.89 | 36.5 |
| | SA | 4.09 | 0.7 | 2.80 | -1.8 |
| 1.0 | $R_{0g}$ | 6.86 | - | 6.06 | - |
| | $R_h$ | 7.18 | 4.6 | 6.49 | 7.1 |
| | $R_{eqCR}$ | 6.76 | -1.5 | 6.12 | 1.0 |
| | $R_{eqV}$ | 6.93 | 1.0 | 6.31 | 4.1 |
| | 3D Plane | 6.77 | -1.4 | 6.21 | 2.5 |
| | SA | 6.76 | -1.5 | 6.16 | 1.7 |

The results under the adiabatic conditions are first examined. For the $NH_3$/air flame at $\phi$=1.0, where the influence of gravity is marginal due to relatively high flame speed, all five approaches accurately measure $S^0_{L,u}$, with $R_h$ showing the largest deviation of only 4.6%. However, with decreasing equivalence ratio, the influence of gravity is increasingly pronounced due to the reduced flame speed, resulting in decreased accuracy, particularly for the methods based on equivalent radii. At $\phi$=0.7, the errors in $S^0_{L,u}$ obtained from $R_h$, $R_{eqCR}$, and $R_{eqV}$ range from 40% to 56%. In contrast, the performance of the $3D\ plane$ and *SA* methods remains acceptable: at $\phi$=0.7, the errors of these two methods are only 6.8% and 5.1% , respectively.

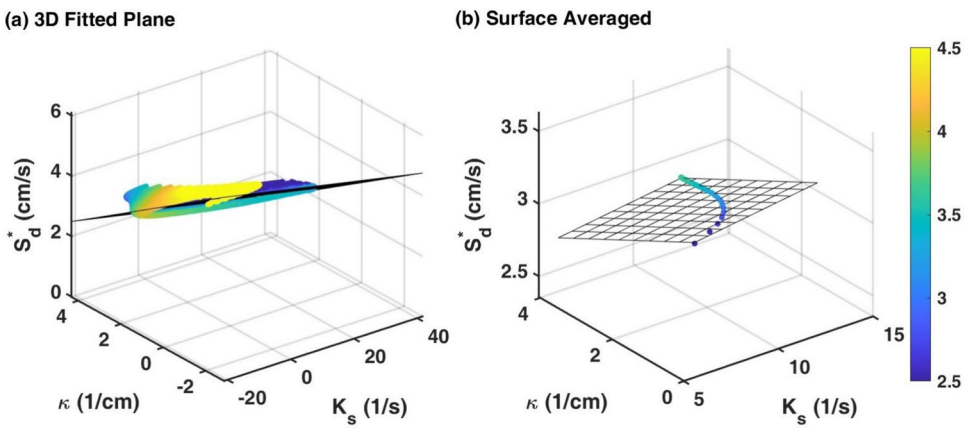


**Fig. 12** Fitting plane from the (**a**) three-dimensional planar fitting method and (**b**) surface-averaged method in the space spanned by density-weighted displacement speed $S^*_d$, strain rate $K_s$, and curvature $\kappa$, for the case of $\phi$=0.8 at the ADI condition

When radiation is considered, as discussed in Section "Combined Effects of Gravity and Radiation", the influence of the inward velocity $u_b$ must be accounted for in the spherically expanding flame method. To this end, the correlation between $u_b$ and the stretch rate $K$ is first extracted from a spherical flame at zero-gravity conditions. Here, $u_b$ is defined as the minimum velocity within the spherical flame, following the method used in Mathew et al. (2025). Then, the $u_b$-$K$ correlation obtained from the zero-gravity flame is applied to the gravity-deformed flames to obtain a corrected $S_{L,b}$-$K$ curve, where $S_{L,b}$ is computed as:

$$S_{L,b} = \frac{dR}{dt} - u_b \tag{19}$$

To underscore the importance of the inflow velocity, Fig. 13 plots the variation of the normalized inflow velocity $u_b/S_{L,b}$ versus flame radius $r$ at the gravity-free conditions. The figure shows that $u_b$ is opposite to the flame-propagation direction and, during steady propagation, reaches roughly one-tenth of the burned flame speed $S_{L,b}$. This indicates that the inflow velocity is non-negligible when measuring the laminar flame speed of $NH_3$/air flames at radiational conditions.

Using the corrected $S_{L,b}$-$K$ curve, the subsequent procedures to obtain $S^0_{L,u}$ remain unchanged. It should be noted that for the $3D\ plane$ and $SA$ methods, the above correction is not required, as these methods inherently account for flame deformation.

The last two columns of Table 3 list the $S^0_{L,u}$ values obtained under radiational conditions. Since a steadily propagating radiative flame in zero-gravity environment does not exist for $\phi$ = 0.7, the corresponding results are omitted. Overall, the inclusion of radiation reduces the accuracy of different approaches. This is because radiation slows flame propagation, thereby enhancing the influence of gravity, as explained in Section "Combined Effects of Gravity and Radiation". Specifically, at $\phi$=1.0, except for $R_{eqCR}$ whose error is slightly reduced, all the others exhibit slightly increased errors, with $R_h$ showing the largest deviation of 7.1%. In contrast, at $\phi$ = 0.8, the errors of $R_h$, $R_{eqV}$, and the $3D\ plane$ method increase substantially from less than 5% to over 20%. Even for $R_{eqCR}$, the error rises from -2.8% to 6.7%. Only the $SA$ method maintains good performance, with a minimal error of -1.8%.

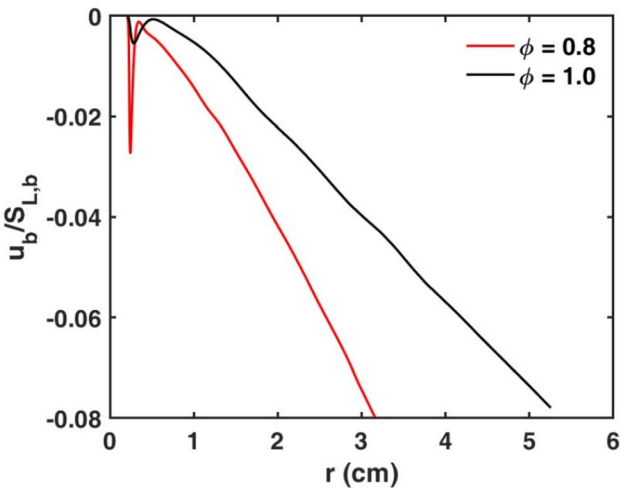


**Fig. 13** Variation of inflow velocity $u_b$ normalized by burned flame speed $S_{L,b}$ versus flame radius $R$ for cases $\phi$ = 0.8 and 1.0 at zero-gravity and radiational conditions

In summary, the above results clearly demonstrate the impacts of gravity and radiation on the measurement of $S^0_{L,u}$ using different approaches. In the absence of radiation effects, the spherically expanding flame method based on different equivalent radii remains accurate when gravity effects are moderate. However, as gravity effects become stronger the spherically expanding flame method is no longer applicable, whereas the $3D\ plane$ and $SA$ methods continue to perform well. Under conditions where both gravity and radiation effects are pronounced, the accuracy of the $3D\ plane$ method deteriorates considerably, leaving the $SA$ method as the only reliable approach for accurately measuring $S^0_{L,u}$.

## Conclusions

In this study, two-dimensional numerical simulations with detailed chemistry and transport are conducted to investigate the propagation of spherically expanding $NH_3$/air flames under gravitational and radiational conditions. Three equivalence ratios of $\phi$ = 0.7, 0.8, and 1.0 are considered. The focus is on examining the influences of gravity and radiation on $NH_3$/air flame propagation and on assessing the accuracy of different approaches for determining the unstretched flame speed $S^0_{L,u}$ from spherically expanding flames.

Results show that gravity significantly deforms the flame front, leading to a mushroom-shaped structure as the flame rises. The deformation becomes more pronounced at lower equivalence ratios due to the reduced flame speed. In addition, the local flame displacement speed is strongly altered by the local flame stretch rate. Since the Markstein number of these flames are positive, the local flame speed increases in the concave region where the flame is negatively stretched, while it decreases near the upper tip region where the flame is positively stretched. Nevertheless, gravity overall accelerates the global flame propagation. In contrast, radiation reduces the flame propagation speed by lowering the flame temperature and

inducing an inward flow velocity. This makes the flame more susceptible to the influence of gravity, resulting in greater deformation of the flame front.

Regarding the measurement of flame speed, it is found that the spherically expanding flame methods based on different equivalent radii remain accurate when the effects of gravity and radiation are moderate. However, when gravity effects become strong, these methods are no longer applicable, while the $3D\ plane$ and $SA$ methods still exhibit good performance. Under conditions where both gravity and radiation effects are pronounced, the accuracy of the $3D\ plane$ method deteriorates considerably, leaving the $SA$ method as the only reliable approach for accurately measuring $S^0_{L,u}$.

The findings from this work enhance the understanding of $NH_3$/air flame dynamics in gravitational and radiative environments and provide valuable guidance for the accurate measurement of the unstretched laminar flame speed of $NH_3$ /air mixtures.

**Author Contributions** S.Z.: Methodology, Investigation, Formal analysis, Writing - original draft, Writing - review and editing. Y.W.: Investigation, Formal analysis, Writing - original draft, Writing - review and editing. S. W.: Conceptualization, Supervision, Resources, Writing - review and editing. Z. C.: Conceptualization, Supervision, Writing - review and editing.

**Funding** This work was supported by National Natural Science Foundation of China (No. 22350710788), the National Key Research and Development Program of China (No. 2025YFF0511801), and the Space Application System of China Manned Space Program under project "Ignition Mechanism of Premixed Near-Limit Flames under Microgravity Conditions".

**Data Availability** The data are available at request.

## Declarations

**Competing Interests** The authors declare no competing interests.

**Ethics Approval** Not applicable.

**Consent for Publication** Not applicable.

**Consent to Participate** Not applicable.

## References

Bechtold, J., Matalon, M.: The dependence of the markstein length on stoichiometry. Combust. Flame **127**(1–2), 1906–1913 (2001)

Berger, L., Hesse, R., Kleinheinz, K., Hegetschweiler, M.J., Attili, A., Beeckmann, J., Linteris, G.T., Pitsch, H.: A dns study of the impact of gravity on spherically expanding laminar premixed flames. Combust. Flame **216**, 412–425 (2020)

Candel, S.M., Poinsot, T.J.: Flame stretch and the balance equation for the flame area. Combust. Sci. Technol. **70**(1–3), 1–15 (1990)

Chen, Z.: Effects of radiation and compression on propagating spherical flames of methane/air mixtures near the lean flammability limit. Combust. Flame **157**(12), 2267–2276 (2010)

Chen, Z.: On the accuracy of laminar flame speeds measured from outwardly propagating spherical flames: Methane/air at normal temperature and pressure. Combust. Flame **162**(6), 2442–2453 (2015)

Chen, Z., Burke, M.P., Ju, Y.: Effects of lewis number and ignition energy on the determination of laminar flame speed using propagating spherical flames. Proc. Combust. Inst. **32**(1), 1253–1260 (2009)

Chen, X., Liu, Q., Jing, Q., Mou, Z., Shen, Y., Huang, J., Ma, H.: Flame front evolution and laminar flame parameter evaluation of buoyancy-affected ammonia/air flames. Int. J. Hydrogen Energy **46**(77), 38504–38518 (2021)

Choi, B.C., Park, J.S., Ghoniem, A.F.: Characteristics of outwardly propagating spherical flames of r134a (c2h2f4)/ch4/o2/n2 mixtures in a constant volume combustion chamber. Energy **95**, 517–527 (2016)

Clavin, P.: Dynamic behavior of premixed flame fronts in laminar and turbulent flows. Prog. Energy Combust. Sci. **11**(1), 1–59 (1985)

Clavin, P., Graña-Otero, J.C.: Curved and stretched flames: the two markstein numbers. J. Fluid Mech. **686**, 187–217 (2011)

Curtiss, C.F., Hirschfelder, J.O.: Transport properties of multicomponent gas mixtures. J. Chem. Phys. **17**(6), 550–555 (1949)

Dowdy, D.R., Smith, D.B., Taylor, S.C., Williams, A.: The use of expanding spherical flames to determine burning velocities and stretch effects in hydrogen/air mixtures. In: Symposium (International) on Combustion, **23**, pp. 325–332 (1991). Elsevier

Faghih, M., Valera-Medina, A., Chen, Z., Paykani, A.: Effect of radiation on laminar flame speed determination in spherically propagating nh3-air, nh3/ch4-air and nh3/h2-air flames at normal temperature and pressure. Combust. Flame **257**, 113030 (2023)

Faghih, M., Chen, Z.: The constant-volume propagating spherical flame method for laminar flame speed measurement. Science Bulletin. **61**(16), 1296–1310 (2016)

Fernández-Tarrazo, E., Gómez-Miguel, R., Sánchez-Sanz, M.: Minimum ignition energy of hydrogen-ammonia blends in air. Fuel **337**, 127128 (2023)

Gaucherand, J., Laera, D., Schulze-Netzer, C., Poinsot, T.: Intrinsic instabilities of hydrogen and hydrogen/ammonia premixed flames: Influence of equivalence ratio, fuel composition and pressure. Combust. Flame **256**, 112986 (2023)

Giannakopoulos, G.K., Gatzoulis, A., Frouzakis, C.E., Matalon, M., Tomboulides, A.G.: Consistent definitions of "flame displacement speed" and "markstein length" for premixed flame propagation. Combust. Flame **162**(4), 1249–1264 (2015)

Glarborg, P., Miller, J.A., Ruscic, B., Klippenstein, S.J.: Modeling nitrogen chemistry in combustion. Prog. Energy Combust. Sci. **67**, 31–68 (2018)

Glaznev, R., Schwenzer, C., Hesse, R., Girhe, S., Halter, F., Chauveau, C., Pitsch, H., Beeckmann, J.: Ultra-slow ammonia flame speeds — a microgravity study on radiation. Proc. Combust. Inst. **40**, 105334 (2024)

Goodwin, D.G., Speth, R.L., Moffat, H.K., Weber, B.W.: Cantera: An object-oriented software toolkit for chemical kinetics, thermodynamics, and transport processes. Zenodo. (2018)

Hayakawa, A., Goto, T., Mimoto, R., Arakawa, Y., Kudo, T., Kobayashi, H.: Laminar burning velocity and markstein length of ammonia/air premixed flames at various pressures. Fuel **159**, 98–106 (2015)

Hindmarsh, A.C., Brown, P.N., Grant, K.E., Lee, S.L., Serban, R., Shumaker, D.E., Woodward, C.S.: Sundials: Suite of nonlinear and differential/algebraic equation solvers. ACM Trans. Math. Softw. (TOMS). **31**(3), 363–396 (2005)

Joulin, G., Mitani, T.: Linear stability analysis of two-reactant flames. Combust. Flame **40**, 235–246 (1981)

Kiverin, A., Yakovenko, I., Melnikova, K.: On the structure and stability of ultra-lean flames. In: Journal of Physics: Conference Series, **1147**, p. 012048 (2019). IOP Publishing

Kobayashi, H., Hayakawa, A., Somarathne, K.K.A., Okafor, E.C.: Science and technology of ammonia combustion. Proc. Combust. Inst. **37**(1), 109–133 (2019)

Law, C., Chung, S., Srinivasan, N.: Gas-phase quasi-steadiness and fuel vapor accumulation effects in droplet burning. Combust. Flame **38**, 173–198 (1980)

Lhuillier, C., Brequigny, P., Lamoureux, N., Contino, F., Mounaim-Rousselle, C.: Experimental investigation on laminar burning velocities of ammonia/hydrogen/air mixtures at elevated temperatures. Fuel **263**, 116653 (2020)

Mathew, J., Tavares, J.K., Jayachandran, J.: Accurately measuring slowly propagating flame speeds: Application to ammonia/air flames. Combust. Flame **271**, 113807 (2025)

Müller, U., Bollig, M., Peters, N.: Approximations for burning velocities and markstein numbers for lean hydrocarbon and methanol flames. Combust. Flame **108**(3), 349–356 (1997)

Okafor, E.C., Hayakawa, A., Nagano, Y., Kitagawa, T.: Effects of hydrogen concentration on premixed laminar flames of hydrogen-methane-air. Int. J. Hydro. Energy **39**(5), 2409–2417 (2014)

Pitsch, H.: The transition to sustainable combustion: Hydrogen-and carbon-based future fuels and methods for dealing with their challenges. Proc. Combust. Inst. **40**(1–4), 105638 (2024)

Poinsot, T., Veynante, D.: Theoretical and Numerical Combustion. RT Edwards, Inc., (2005)

Ronney, P.D.: Understanding combustion processes through microgravity research. In: Symposium (International) on Combustion, **27**, pp. 2485–2506 (1998). Elsevier

Shrestha, K.P., Lhuillier, C., Barbosa, A.A., Brequigny, P., Contino, F., Mounaim-Rousselle, C., Seidel, L., Mauss, F.: An experimental and modeling study of ammonia with enriched oxygen content and ammonia/hydrogen laminar flame speed at elevated pressure and temperature. Proc. Combust. Inst. **38**(2), 2163–2174 (2021)

Sun, C., Sung, C.-J., He, L., Law, C.-K.: Dynamics of weakly stretched flames: quantitative description and extraction of global flame parameters. Combust. Flame **118**(1–2), 108–128 (1999)

Takizawa, K., Takahashi, A., Tokuhashi, K., Kondo, S., Sekiya, A.: Burning velocity measurements of nitrogen-containing compounds. J. Hazard. Mater. **155**(1–2), 144–152 (2008)

Tavares, J.K., Gururajan, V., Jayachandran, J.: Effects of radiation heat loss on planar and spherical hydrofluorocarbon/air flames. Combust. Flame **258**, 113067 (2023)

Thiesset, F., Halter, F., Bariki, C., Lapeyre, C., Chauveau, C., Gökalp, I., Selle, L., Poinsot, T.: Isolating strain and curvature effects in premixed flame/vortex interactions. J. Fluid Mech. **831**, 618–654 (2017)

Vervisch, L., Bidaux, E., Bray, K., Kollmann, W.: Surface density function in premixed turbulent combustion modeling, similarities between probability density function and flame surface approaches. Phys. Fluids **7**(10), 2496–2503 (1995)

Wang, Y., Guan, X., Xie, S., Zhou, M., Zhang, Z., Chen, Z., Zhang, T.: Numerical studies on the ignition and propagation for spherically expanding premixed cool flames under gravitational conditions. Combust. Flame **259**, 113194 (2024)

Wang, Y., Han, W., Attili, A., Chen, Z.: Numerical analysis of very rich propagating spherical flames: Soot formation and its impact on the determination of laminar flame speed. Combust. Flame **237**, 111860 (2022)

Wu, J.-Z., Ma, H.-Y., Zhou, M.-D.: Vortical Flows, vol. 28. Springer, Heidelberg (2015)

Xie, S., Zhang, H.: On the extinction and burning limits of stretched premixed ammonia flames at elevated pressures. Combust. Flame **279**, 114248 (2025)

Yakovenko, I., Ivanov, M., Kiverin, A., Melnikova, K.: Large-scale flame structures in ultra-lean hydrogen-air mixtures. Int. J. Hydro. Energy **43**(3), 1894–1901 (2018)

Yakovenko, I., Kiverin, A., Melnikova, K.: Ultra-lean gaseous flames in terrestrial gravity conditions. Fluids. **6**(1), 21 (2021)

Yao, M.X., Blanquart, G.: Isolating effects of large and small scale turbulence on thermodiffusively unstable premixed hydrogen flames. Combust. Flame **269**, 113657 (2024)

Yu, D., Chen, Z.: Premixed flame ignition: Theoretical development. Prog. Energy Combust. Sci. **104**, 101174 (2024)

Yu, H., Han, W., Santner, J., Gou, X., Sohn, C., Ju, Y., Chen, Z.: Radiation-induced uncertainty in laminar flame speed measured from propagating spherical flames. Combust. Flame **161**, 2815–2824 (2014)

Zhou, C., Liang, W., Chen, Z.: On explosion limits of ammonia-oxygen mixtures with hydrogen addition: sensitivity and nonmonotonicity. Energy & Fuels. **35**(17), 14035–14041 (2021)

Zirwes, T., Zhang, F., Habisreuther, P., Hansinger, M., Bockhorn, H., Pfitzner, M., Trimis, D.: Quasi-dns dataset of a piloted flame with inhomogeneous inlet conditions. Flow Turbul. Combust. **104**(4), 997–1027 (2020)

Zitouni, S., Brequigny, P., Mounaim-Rousselle, C.: Influence of hydrogen and methane addition in laminar ammonia premixed flame on burning velocity, lewis number and markstein length. Combust. Flame **253**, 112786 (2023)